Research Article | Vol. 10, No. 8 / 1 August 2019 / Biomedical Optics Express 3963

Biomedical Optics EXPRESS

Novel methodology to image stromal tissue and assess its morphological features with polarized light: towards a tumour microenvironment prognostic signature

JARED WESTREICH,[1] MOHAMMADALI KHORASANI,[2] BLAKE JONES,[1] VALENTIN DEMIDOV,[1] SHARON NOFECH-MOZES,[3] AND ALEX VITKIN[1,4,5,*]

[1] *Department of Medical Biophysics, University of Toronto, Toronto, Canada*
[2] *Fellow, Department of General Surgical Oncology, University of Toronto, Toronto, Canada*
[3] *Department of Laboratory Medicine and Pathobiology, University of Toronto, Toronto, Canada*
[4] *Division of Biophysics and Bioimaging, Princess Margaret Cancer Centre, University Health Network, Toronto, Canada*
[5] *Department of Radiation Oncology, University of Toronto, Toronto, Canada*
[*] *Alex.Vitkin@rmp.uhn.ca*

Abstract: The amount and organization details of peri-tumoural stroma have been linked to patient outcomes in various cancers. In this study, we propose a novel and relatively simple methodology using polarized light microscopy (PLM) to image fibrillar structures within a tumour microenvironment, using only linear crossed polarizers. We demonstrate the technique's ability to image and extract measurement-geometry-independent quantitative morphological metrics related to stromal density and alignment in human invasive breast cancer samples. The findings are promising towards quantitative characterization of peri-tumoural stroma, with potential to develop a PLM signature of tumour microenvironment for providing clinically important information such as breast cancer behaviour or treatment outcome prognosis.

© 2019 Optical Society of America under the terms of the OSA Open Access Publishing Agreement

1. Introduction

The study of peri-tumoural compartments and their interactions with the tumour has been a long-standing topic in oncological research. It has been hypothesized and demonstrated that the interplay between the tumour and its surrounding host environment, called tumour microenvironment (TME), can play an important role in cancer behaviour and its response to therapy [1–3]. The stroma surrounding tumour cells, designated as peri-tumoural stroma, is composed of various cell types and extra-cellular matrices that facilitate signalling pathways and can affect tumour formation, progression, and patient outcomes [1,4]. Extracellular matrix (ECM), a component of peri-tumoural stroma, is a complex composition of fibres that can play an important role in tumour behaviour. For instance, the production of growth factors by tumour cells can lead to remodelling of ECM [1,2] leading to peri-tumoural stroma which is frequently disorganized and desmoplastic. The cross linking between ECM collagen fibres is believed to enhance certain signalling pathways, such as PI3 K, contributing indirectly to tumour progression [3].

Peri-tumoural stroma itself has been shown to contain clinically important information. For instance, gene-expression profiles of stroma in breast cancer has been linked to response to chemotherapy [5]. In rectal cancer, histologically-derived morphological categorization of fibrotic tumour stroma has been developed and correlation with patient prognosis is being explored [6]. In cholangiocarcinoma, the fibrotic stroma scoring nomograms have been proposed as a prognostic tool as well [7]. In breast cancer, it has been observed that more mammographic dense

#364523 https://doi.org/10.1364/BOE.10.003963
Journal © 2019 Received 12 Apr 2019; revised 26 May 2019; accepted 24 Jun 2019; published 15 Jul 2019

Biomedical Optics EXPRESS

breast tissues, containing more extensive connective tissue are associated with worse outcomes [8]. Further, it has been suggested that the amount of peri-tumoural stroma in breast cancer, quantified via tumour-to-stroma ratio, correlates with risk of local recurrence, distant metastasis, and patient survival [8–13].

Pathologists often describe peri-tumoural stroma features qualitatively, partly due to the lack of standard guidelines for evaluation of ECM. The challenges in effectively quantifying peri-tumoural stroma features have been a barrier to a better understanding of their correlation to tumour behaviour and patient outcomes. In addition to histological approaches, a recent study using second harmonic generation imaging in early gastric cancer specimens were used to extract and quantify morphological and texture features of peri-tumoural collagen to derive collagen signatures that correlated with lymph node metastasis in this clinical cohort [15]. This study suggests that important information is indeed contained in the peri-tumoural stroma, with potential clinical translation if its features can be robustly measured and quantified.

Polarized light microscopy (PLM) is a promising modality to image breast cancer and its stromal compartment because it yields rich and relatively unexplored biophysical information content [16,17]. Due to its intrinsic tissue contrast, PLM requires minimal sample preparation. Its widefield nature enables visualization of large tissue regions, with rapid image acquisition and processing times. There are several implementations of PLM, ranging from very simple to more complex, with the latter providing a wealth of rich quantitative data [15,16]. PLM has long been used to image stroma because it is made up of many structures (e.g., collagen and elastin fibres [17,18]) which interact strongly with polarized light due to their birefringence [17]. For example, orientation and alignment of pancreatic cancer ECM fibres imaged with PLM has been shown to correlate well with second harmonic generation, a gold standard for fibrillar collagen imaging [19].

Traditionally, the simplest PLM implementation has involved looking at samples through cross polarizers. Since transmitted light intensity of a birefringent structure viewed between crossed polarizers is orientation dependent, in a given image only a subset of structures within a small range of orientations will be visible [20]. Thus, all birefringent tissue structures, typically oriented in a variety of directions, cannot be quantified in a single crossed-linear-polarizers image. More advanced implementations of PLM that derive measurement-geometry-independent sample information, such as the Mueller matrix (MM) and the LC-Polscope approaches (an instrument and image processing methodology), can calculate birefringence and structure orientation [16,21]. However, complexity of MM and LC-PolScope motivates the development of PLM methodologies that give robust quantitative data, while remaining practical and simple.

In this study, we describe an alternative novel polarization technique for imaging and quantifying human breast cancer slides using a relatively simple and robust implementation of PLM and demonstrate initial results for quantitative peri-tumoural stroma assessment. We then discuss the advantages and limitations of this methodology as a potentially promising approach to study peri-tumoural stromal component of tumour microenvironment.

2. Materials and methods

2.1. Human breast cancer samples

Institutional ethics approval was obtained from participating hospital institutions (University Health Network and Sunnybrook Hospital, both in Toronto, Canada). Need for patients' consent to use the breast cancer histology samples was waived by the ethics board due to the retrospective nature of the study and anonymization of the information.

Unstained formalin fixed paraffin embedded invasive breast cancer histology slides of 4.5 µm thickness were imaged using the PLM technique described below. Prior to imaging, the samples were dewaxed from paraffin to minimize possible polarization artefacts [22]. All samples were

Biomedical Optics EXPRESS

from invasive breast cancer surgical specimens, in patients with no history of treatment with chemotherapy or radiation to breast prior to surgery.

We imaged representative sections of peri-tumoural stroma from 5 invasive ductal carcinoma patients and extracted quantitative PLM metrics describing the density and alignment of stromal regions. Using an adjacent Haematoxylin and Eosin (H&E) stained histology section, a pathologist blinded to PLM results chose four 200 µm x 200 µm regions of interest (ROIs) per slide to demarcate areas for each of 1) high alignment, 2) low alignment, 3) high density, and 4) low density of fibrillar stroma. For the purpose of this designation, histological alignment was assessed as relative abundance of parallel stromal fibres, and density as the relative absence of spaces between stromal fibres. The degree of alignment or density was relative to each individual slide. Areas containing epithelial elements (benign, *in situ* or invasive carcinoma), adipose tissue, biopsy site reaction ("needle tract") and stroma with dense inflammatory infiltrate were excluded. We then compared our quantified PLM-derived metrics in the corresponding areas of PLM images to the pathologist's assessment, to evaluate the ability of PLM to correctly identify these important ECM characteristics.

2.2. Polarized light microscopy system

We implemented a homemade PLM module onto a commercial stereo zoom microscope operating in transmission mode (Axio Zoom V16, Zeiss) with a LED white light illumination source. The module consisted of input and output polarizers (the latter called the analyzer; both LPVISE100-A, Thorlabs) oriented perpendicularly to each other and placed in individual motorized angular rotation mounts (PRM1/MZ8, Thorlabs) on either side of the tissue sample. Electromechanical mount controllers (KDC101, Thorlabs) were connected to a computer, with rotation enabled via a LabVIEW program; the crossed polarizers were rotated synchronously to 36 different angular positions about the microscope transmission axis. Images were acquired at 20x (and 80x) magnification, with a field of view of 6.4 mm x 6.4 mm (1.6 mm x 1.6 mm) and a pixel size of 3.1 µm square (0.8 µm square). The total measurement time to acquire the 36 angular images was 180 seconds.

2.3. Measurement and analysis technique

There will be no transmission through crossed linear polarizers unless a polarization-active material is placed between the orthogonal pair [23]. Thus, a birefringent sample exhibiting direction-dependent index of refraction will be visible under crossed polarizers. Birefringence arises due to direction-dependent asymmetry of the refractive index at the molecular scale (intrinsic birefringence) or when asymmetric structures, such as collagen fibres, with a given refractive index, are embedded within a background material with a different refractive index (form birefringence) [17]. Its visibility relative to background will depend on the actual birefringence value Δn (refractive index difference between the 'fast' and 'slow' (birefringent) axes of the material) and on its orientation relative to the crossed polarizers. A representative breast cancer slide image is shown in Fig. 1(a), highlighting a subset of birefringent tissue structures that transmit at this particular crossed-polarizers orientation. Then, as the angle between the birefringent axis of the sample and the crossed polarizers is changed (by rotating the sample, which is difficult in practice; or by rotating the crossed polarizer-analyzer pair, as pursued below), its visibility will oscillate in a periodic sinusoidal fashion [24]. Mathematically, the brightness L of the birefringent structure is given by:

$$L = 100\% \times \left\{ \sin^2(2\tau) \times \sin^2\left[\left(\frac{\Delta n \times t}{\lambda}\right) \times \pi\right]\right\} \tag{1}$$

where τ is the angle between the birefringent axis of the material (e.g., collagen alignment direction) and the input polarizer orientation, t is the sample thickness, and λ is the wavelength of

Biomedical Optics EXPRESS

light [24]. Thus, for a given birefringent tissue structure, the brightness will vary with angle as:

$$L \sim \sin^2(2\tau) \tag{2}$$

exhibiting a maximum at $\tau = 45^{o}$ and an oscillation period of 90°. This relationship applies for both intrinsic and form birefringence. For our study, the crossed polarizer-analyzer pair was rotated about the breast cancer sample in 5° increments; we oversampled by obtaining 36 images over 180° range for enhancing signal-to-noise ratio (SNR). We then removed the slide and re-imaged at each orientation to get the flood-field correction for each image. Representative variations from an aligned ECM region and a cellular tumour region are shown in Fig. 1(b). As seen, a highly birefringent aligned ECM (collagen) structure exhibits higher average brightness and greater oscillation in visibility compared to the cellular core of the tumour. We use these differences to derive higher-contrast and measurement-angle-independent PLM stroma images of tumour density and alignment, and extract quantitative ECM metrics, as below.

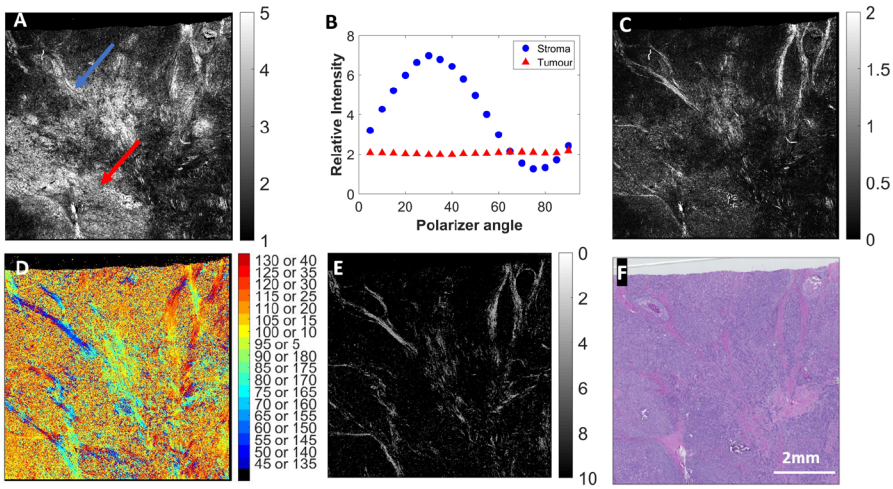

Fig. 1. Signal processing workflow showing various types of PLM images with improved contrast between tumour and intratumoural stroma, using an invasive human ductal carcinoma as an illustrative example. A) A single cross polarization image at 20x magnification. Only stroma aligned at certain orientations can be seen; other structures, possibly in the tumour cellular compartment, are also visible. The contrast between the two tissue types is modest. B) The relative intensity as a function of measurement angle for a representative pixel of stromal and tumour tissues (blue and red arrows in A), respectively) Stroma contains fibrous structures that are birefringent, so the intensity of pixels corresponding to these areas is higher and varies significantly; conversely, tumour regions are less birefringent and more random / heterogenous, with resultant intensities and its variation significantly lower. C) A standard deviation (SD) image of the angular oscillations in B), now yielding a higher-contrast, measurement-angle-independent image compared to A). Certain stromal regions become more visible while the brightness of others (tumour cellular compartment) is diminished. D) A direction image where the colour at each pixel (derived from the polarizer measurement angle that yielded the highest intensity) displays the relative fibre orientation at that pixel. E) An alignment image derived from D), based on the amount of directional variation in nearest-neighbour pixels (for details, see text). F) Corresponding H&E histology, with stromal regions in pink reddish hues, and tumoural masses in darker purple. Good qualitative agreement is seen with the derived parametric PLM images of stromal *density* in C) and stromal *alignment* in E). The 2 mm scale bar in F) applies to all images in this figure.

Biomedical Optics EXPRESS

2.4. Signal processing and stromal metrics derivation

Among the several possible image processing approaches to highlight the presence of aligned birefringent structures in fibrillary stroma, we closely examined the angular oscillations graph of Fig. 1(b) and came up with the following. For each pixel we calculated the standard deviation (SD) of the brightness over all 36 measurement angles and generated the resulting parametric SD images as shown in Fig. 1(c). These exhibit improved contrast between tumour and stroma, and importantly are independent of the asymmetry / directionality orientation of the latter. Tumour is less birefringent and thus exhibits smaller intensity levels, which vary less as a function of measurement angle, thus yielding lower SD values. Conversely, many of the stromal components (e.g., aligned collagen and elastin fibres) appear bright at some measurement angles, and quite dark on others; thus, their larger oscillation amplitude yields higher SD values. Therefore, the resultant SD images display good contrast between tumour and stroma (Fig. 1(c).), and their brightness can be used to quantitate the relative abundance (*density*) of connective tissues.

Additional signal processing was pursued to arrive at images of stromal alignment. We determined the birefringence orientation at each pixel by selecting the polarizer angle (in the $0° - 90°$ range, see Fig. 1(b).) that exhibited the highest pixel brightness. According to Eq. (2), for a birefringent structure viewed between crossed polarizers, the transmission will be highest when the polarizer / analyzer pair and structure are offset by 45°. For example, if a structure is brightest when the polarizer is at 60°, the structure's birefringent axis must be at 15° or 105°. The resultant birefringence orientation image is shown in Fig. 1(d)., where the above ambiguity is retained (see double-valued colour bar) for this feasibility study. This ambiguity could be eliminated with the addition of a compensator [21], but was omitted at this stage for simplicity.

To derive a more robust representation of local tissue alignment, we checked whether individual neighbouring pixels in each region of Fig. 1(d). had birefringent axis orientations in similar directions. Specifically, we calculated the alignment by computing the mean angular difference among neighbouring pixels. We generated an alignment image using a 5×5 pixel sliding window extending 2 pixels left, right, up, and down centered at the calculation pixel. This window size was chosen to be sufficiently large for a reasonable SNR and averaging statistics, while being small enough to avoid significant blurring in the resultant alignment image. This resultant window size (~4 µm x 4 µm with our microscope resolution at 80x magnification) is also of biologically-relevant spatial scale as most collagen fibre diameters [25]. To overcome the tissue orientation angle ambiguity mentioned above, we used circular statistics in calculating the angular mean. Briefly, for any pair of pixels, the smallest angular difference was selected (e.g., if one pixel's orientation is 5° or 95° and another is at 85° or 175°, the difference is taken to be 10°). Mathematically,

$$angular\ difference = min\{mod[(\theta_1 - \theta_2), 180°], mod[-(\theta_1 - \theta_2), 180°]\} \tag{3}$$

where θ_1 and θ_2 are the polarizer angles that resulted in the highest brightness for two nearby pixels.

Then for a window of n pixels (25 in our analysis), the average angular difference was calculated by:

$$mean\ anglular\ difference = \frac{\sum_{i=1}^{n-1} \sum_{j=i+1}^{n} angular\ difference_{ij}}{\frac{n(n-1)}{2}} \tag{4}$$

The value of mean angular difference is then assigned to the center pixel in the window, and the process repeated at all pixels of an orientation image. A low mean angular difference thus indicates a region of high alignment, whereas a large spread in angular orientations signifies a chaotic / randomly aligned region. The resulting regional alignment image of Fig. 1(e). provides an indication of local tissue directional asymmetry and will be used to quantify the degree of

Biomedical Optics EXPRESS

alignment; we expect low values of this metric to indicate regions of highly aligned biological structures (e.g., collagen fibres in stroma).

3. Results

Figure 1(a). shows an image obtained from a single cross polarization measurement. By comparison with the H&E histology in Fig. 1(f)., it is apparent that many of the fibres present in this sample are not visualized. This is because at a single crossed-polarizer measurement position, the brightness of a particular birefringent fibre depends on its orientation relative to the crossed polarizers; thus, some fibres are simply not seen. Furthermore, many "background" areas of tumour exhibit varying degrees of birefringence and depolarization, giving a light-and-dark speckle-like pixelated appearance to the image. Overall then, many areas of ECM are not visible; further, the contrast between the stroma and the tumour is quite modest.

By processing the images from multiple crossed-polarizer measurement angles, we generate a measurement-orientation-independent increased-contrast tissue image that visualizes more of the stroma and suppresses the tumour cellular compartment (Fig. 1(c).). The improvement stems from the difference in birefringence between the two tissue types: the fibrillar stroma is made primarily of birefringent fibres and so its brightness, over multiple measurement angles, oscillates with a high amplitude which yields a high standard deviation value pixel on an SD image. Conversely, tumour cells tend to have lower birefringence and their contribution to brightness, perhaps from the depolarization process, is lower and does not vary strongly with measurement angle. This results in a significantly lower SD value for pixels containing tumour.

Figure 1(d). shows an orientation image whereby each pixel's colour is indicative of tissue's birefringent axis direction. Therefore, aligned structures such as stromal fibres appear as regions with similar colour, changing only when the orientation of the fibres changes. Tumour regions, however, exhibit strong heterogeneity in birefringent axis direction, and thus display significant local colour variations in this image. Conceptually this makes sense as a pixel representing tumour may be birefringent due to any small asymmetric / aligned structures within a tumour cell, and thus exhibit some signal; however, it is unlikely that neighbouring birefringent tumour structures will be oriented in the same direction. Capitalizing on this potential distinction between different tissue types, an alignment image was derived to represent the average difference between orientations on the micron spatial scale of the 5×5 pixel neighbourhood around each pixel. The results displayed in Fig. 2(e). show significant improvement in delineating directional stroma structures of ECM.

Table 1. Pathologist categories *versus* PLM scores for density and alignment.

Slide	Pathologist Density Category	PLM Density Score	Agreement?	Pathologist Alignment Category	PLM Alignment Score	Agreement?
1	High	0.41	Yes	High	0.41	Yes
	Low	0.21		Low	0	
2	High	0.45	Yes	High	0.51	Yes
	Low	0.11		Low	0.44	
3	High	0.94	Yes	High	0.99	Yes
	Low	0.91		Low	0.50	
4	High	0.04	No	High	1	Yes
	Low	0.58		Low	0.58	
5	High	1	Yes	High	0.43	Yes
	Low	0		Low	0.35	

Biomedical Optics EXPRESS

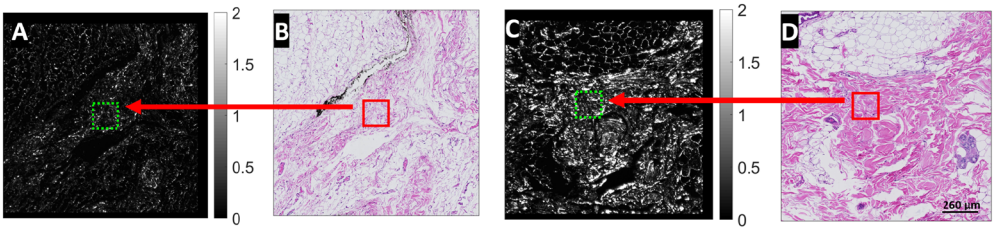

Fig. 2. PLM can differentiate regions of low and high *stromal density* in human breast cancer samples. Following Fig. 1(c)., an illustrative example of breast stroma from a case of human invasive ductal carcinoma slide is shown, designated as Slide 5 in Table 1. A) PLM density image containing regions of low-density stroma. B) H&E histology image from an adjacent section. The red square ROI is chosen by a pathologist, blinded to the polarization images, to indicate an area of low stromal density. This is projected to the PLM density image as the dotted green square in A) for quantification, with results summarized in Table 1. C) PLM density image of an area containing high density stroma. D) Corresponding H&E histology image with a pathologist-marked ROI to indicate a region of high-density stroma, projected as the dotted green square in C).

Thus, we've developed two methods for improved ECM visualization: the SD stromal *density* image of Fig. 1(c). based on the difference in birefringence magnitude, and the stromal *alignment* image of Fig. 1(e). based on differences in birefringence direction. While stemming from quite distinct underlying sources of contrast, both show good visual agreement with histology of Fig. 1(f).

Moving beyond the visual and qualitative comparisons, we now attempt to quantitate the derived PLM stromal density and orientation images. Performing the density analysis first, Fig. 2(a). shows an SD polarization image for a representative human invasive carcinoma sample that exhibits regions of low stromal density; Fig. 2(b). shows the adjacent histological section with an ROI chosen by a pathologist blinded to PLM analysis that marks such a region. The corresponding ROI on the SD image is marked by a dotted green square. Averaging the SD values over all pixels within this 200 µm x 200 µm region results in a stromal density metric, as summarized for all five slides in Table 1. The agreement of the derived PLM metrics for stromal density with the qualitative low / high histological designations, seen in 4 of the 5 examined cases, is encouraging.

Moving on to the stromal alignment analysis, Fig. 3(a). shows a polarization alignment image for a typical human invasive ductal carcinoma sample that exhibits regions of low ECM alignment; Fig. 3(b). shows the adjacent histological section with an ROI chosen by a pathologist blinded to PLM analysis that marks such a region. Averaging the alignment values over the corresponding 200 µm x 200 µm region in Fig. 3(a). yields an alignment metric value; analogous process for the high alignment regions is outlined in Fig. 3(c). and 3(d). Comparison of calculated alignment metrics with pathologist's assignments is summarized for the five slides in Table 1. As seen, there is agreement with pathological designations for all 5 examined cases, another encouraging preliminary finding of our proposed PLM methodology.

Table 1 summarizes the results of the PLM-derived quantitative metrics and the pathologist's designation for density and alignment. Note that the metrics were normalized to be between 0 and 1 (e.g., a density metric of 0 means that ROI had the lowest density, as measured by average SD, of all the ROIs imaged). In four of five slides imaged, the PLM density scores agreed with the pathologist's label. The agreement was stronger (5 out 5) for alignment comparison. Although encouraging, further investigation is necessary to evaluate the method's robustness. For example, although in agreement, the differences between the high- and low-density scores for Slide 3 are small (0.94 *vs* 0.91). Also, the one misclassified sample (density of Slide 4) gives a

Biomedical Optics EXPRESS

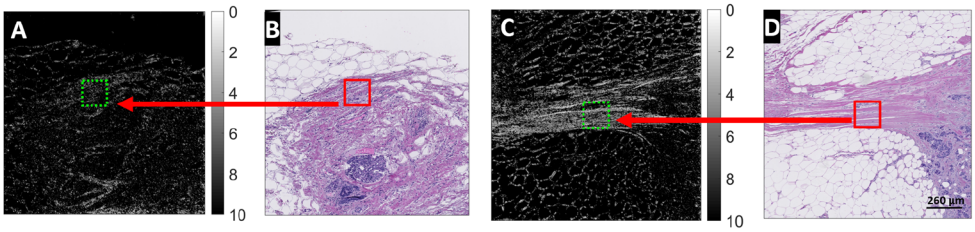

Fig. 3. PLM can differentiate regions of low and high *stromal alignment* in human breast cancer samples. Following Fig. 1(e)., an illustrative example of breast stroma from a case of human invasive ductal carcinoma slide is shown, designated as Slide 1 in Table 1. A) PLM alignment image containing regions of low-alignment stroma. B) H&E histology image from an adjacent section. The red square ROI is chosen by a pathologist, blinded to the polarization images, to indicate an area of low stromal alignment. This is projected to the PLM alignment image as the dotted green square in A) for quantification, with results summarized in Table 1. C) PLM alignment image of an area containing high-alignment stroma. D) Corresponding H&E histology image with a pathologist-marked ROI to indicate a region of high-alignment stroma, projected as the dotted green square in C).

very low score (0.04) for the ROI labeled as high alignment, which is not understood at present. Further work is needed to determine whether this methodology will be significantly affected by inter-sample variations, such as small differences in slide thickness.

4. Discussion

Stroma morphological features such as density and alignment are hypothesized to be important prognostic indicators for cancer, including breast cancer. Certain changes in collagen fibres surrounding breast tumour have been proposed as markers of tumour progression and are referred to as tumour-associated collagen signatures (TACS) [8], describing the alignment and orientation of fibres relative to the cancel cell nests. For example, fibres aligned perpendicular to the tumour, termed TACS-3, are thought to facilitate a path for metastasis and have been shown to inversely correlate with disease-free survival [8]. In addition, higher fibrillar stroma content in peri-tumoural environment has been shown to be associated with worse disease-free survival in breast cancer [8,13]. Pancreatic ductal adenocarcinoma patients with high peri-tumoural stroma density have been shown to have better outcomes than those with intermediate or low stroma density [26]. In rectal cancer, morphological features of fibrous peri-tumoural stroma such as elongation degree and layered structural pattern based on H&E have been incorporated into stroma categorization for correlation with oncological outcomes [6]. These studies highlight the importance of fibrillar stroma morphological features and their potential prognostication value. These findings call for readily accessible and robust methodologies that can quantify such prognostically important stromal morphological features. This will help better understand the interactions between tumour and its microenvironment, and more extensively explore their correlation with tumour behaviour (such as metastatic pattern, recurrence, response to therapy, etc.) and patient prognosis outcomes (such as progression free and overall survival). Here, we propose an experimentally simple PLM methodology with modest signal processing requirements to image peri-tumoural stroma and demonstrate its feasibility to quantify fibrillar stroma morphological features such as density and alignment, as a promising alternative candidate to study tumour microenvironment in solid tumours.

Studies that have demonstrated correlation between stromal components and patient outcomes and tumour behaviour have mostly utilized modalities other than PLM. However, PLM has several advantages making it a suitable candidate for research application and potential clinical translation.

Biomedical Optics EXPRESS

For instance, PLM can be used to image unstained thin pathology slides that are fixed and paraffin embedded. In the context of this study, examination of unstained fixed slides allows for access to large tumour archive databases that can be studied retrospectively as well as prospectively. This is a benefit that many alternative tools (e.g., mass spectrometry) lack. The ability of PLM to image peri-tumoural stroma in fixed tissue also allows the pathologist to examine the subsequent H&E slides and guide the PLM technique to image the most relevant tumour-stroma interface (such as the most "infiltrative front"), a well-known advantage of a prognostication tool [27,28]. One potential disadvantage of PLM is that for exclusively collagen imaging, second harmonic generation is a better choice: PLM visualizes any birefringent structures regardless of their biological origin and as such is not collagen-specific [16]. However, in the context of connective tissue imaging within tumour microenvironment, PLM contains imaging information about several tissue types at once, making it a more encompassing tool when visualizing heterogeneous stroma. On the practical technology front, PLM is widefield, enables rapid image acquisition and processing times, and is implemented with inexpensive and robust optical instrumentation.

The rotating crossed-polarizers PLM variant described here is particularly promising due to its significant information content, simplicity, and ease of implementations. Using only linear polarizer measurements and straight-forward signal processing, this technique can generate an intensity map that captures the network of stromal fibres, along with a map that shows birefringent axis orientation of the stromal tissue structures. Linear polarizers can easily be inserted to the filter wheels of most microscopes. Unlike quarter waveplates, their optical properties remain relatively constant across the visible spectrum and thus can be readily used with most white-light broadband sources. Further, unlike liquid crystal retarders (e.g., as used in the LC-PolScope [21]), they do not vary with temperature nor drift in time and thus do not require calibration. In addition to experimental ease, the relatively simple signal processing steps that convert the angular measurements to high-contrast information-rich density and alignment images compare favorably with complex and labour-intensive image processing inherent in deriving the tissue Mueller Matrix and then performing decomposition analysis to extract biophysical properties [29]. Of course, the very simplicity of this method also results in decreased information content, for example decreased quantitative accuracy in determining sample birefringence (retardance) and orientation as possible with LC-PolScope and MM [16,21]. Although MM gives a complete description of a sample's interaction with polarized light, there may be applications where rotating crossed-polarizers PLM is more appropriate due to its simplicity and ease of implementation, while still enabling sufficiently informative data collection. For example, the standard deviation image provides contrast between tumour and stroma, and therefore may be suitable for automatic segmentation of the tumour compartment within breast tissue samples. Future work will compare the various trade-offs and compromises of different PLM implementations, amongst themselves and relative to the MM "gold standard" and will examine specific applications where a particular variant of rotating crossed-polarizer PLM may prove most suitable.

The next stage of this project will further investigate this methodology's ability to accurately measure tissue orientation and birefringence. Using this PLM approach, we can extract birefringence as follows. First, as shown above, the polarizer angle yielding the highest intensity is determined at each pixel (this should occur at $\tau = 45°$). Then Eq. (1) is rearranged to yield birefringence Δn:

$$\Delta n = \sin^{-1}\left(\sqrt{\frac{L}{100\%}}\right) \times \frac{\lambda}{t \times \pi} \tag{5}$$

We will compare the resultant Δn values and their axis orientations with LC-PolScope, which has been shown to be effective for measuring these properties in thin tissues [30]. We will investigate image sampling with smaller angular intervals, such as every 1° (instead of 5° currently) to estimate stromal orientation more precisely. We will also integrate rotating polarizers into a

Biomedical Optics EXPRESS

microscope with higher magnification as to analyze stroma on a smaller spatial scale. We also plan to investigate a larger and more diverse set of human breast cancer samples.

In addition to ECM density and alignment as per this initial demonstration, we will draw upon more advanced image processing techniques to extract other morphological features such as fibre length / elongation, width, and tortuosity. We will also extract texture features from density and orientation images using the Gray Level Co-occurrence Matrix (GLCM), which analyzes the spatial relationship of neighbouring pixels and yields additional interesting texture features such as contrast, correlation, energy, and homogeneity. With quantification of all these PLM-derived metrics, we will explore a PLM signature with correlation to patient outcomes. We also note that the proposed PLM methodology is not limited to imaging peri-tumoural breast stroma and can be explored in other solid tumours such as colorectal, gastric, pancreatic and biliary carcinomas and prostate cancer, where the value of studying morphological and density features of the stroma has been demonstrated based on H&E histological assessments [5–7,12,14,15,26,31,32]. Beyond cancer and life sciences applications, a rapid and simple method to image aligned structures can be applicable in other fields such as mineralogy and material sciences.

5. Conclusion

We have described a simple and robust PLM measurement and signal processing methodology to image peri-tumoural stroma and extract quantitative metrics that characterize this component of tumour microenvironment, with an eye towards an eventual PLM signature to help predict tumour behaviour and patient prognosis. From simple cross-polarizers measurements as several angles relative to the tissue sample, we show how to obtain parametric polarization images that highlight connective tissue density and alignment. In a small study of human breast cancer samples, quantitative metrics derived from these images agree well with independent histological assessment. The proposed PLM methodology holds promise to extract and quantify important information about fibrillar peri-tumoural stroma for the study of tumour microenvironment, and further investigations of this approach appear warranted.

Funding

Canadian Institutes of Health Research (CIHR) (PJT-156110).

Acknowledgments

The authors thank Adam Gribble, along with James Jonkman and his team at the Advanced Optical Microscopy Facility (Toronto) for help with the PLM module.

Disclosures

The authors declare that there are no conflicts of interest related to this article.

References

1. M. M. Mueller and N. E. Fusenig, "Friends or foes - Bipolar effects of the tumour stroma in cancer," Nat. Rev. Cancer **4**(11), 839–849 (2004).
2. D. Hanahan and L. M. Coussens, "Accessories to the crime: functions of cells recruited to the tumor microenvironment," Cancer Cell **21**(3), 309–322 (2012).
3. M. R. Junttila and F. J. De Sauvage, "Influence of tumour micro-environment heterogeneity on therapeutic response," Nature **501**(7467), 346–354 (2013).
4. K. R. Levental, H. Yu, L. Kass, J. N. Lakins, M. Egeblad, J. T. Erler, S. F. T. Fong, K. Csiszar, A. Giaccia, W. Weninger, M. Yamauchi, D. L. Gasser, and V. M. Weaver, "Matrix crosslinking forces tumor progression by enhancing integrin signaling," Cell **139**(5), 891–906 (2009).
5. P. Farmer, H. Bonnefoi, P. Anderle, D. Cameron, P. Wirapati, V. Becette, S. André, M. Piccart, M. Campone, E. Brain, G. MacGrogan, T. Petit, J. Jassem, F. Bibeau, E. Blot, J. Bogaerts, M. Aguet, J. Bergh, R. Iggo, and M. Delorenzi, "A

Biomedical Optics EXPRESS

stroma-related gene signature predicts resistance to neoadjuvant chemotherapy in breast cancer," Nat. Med. **15**(1), 68–74 (2009).
6. H. Ueno, A. M. Jones, K. H. Wilkinson, J. R. Jass, and I. C. Talbot, "Histological categorisation of fibrotic cancer stroma in advanced rectal cancer," Gut **53**(4), 581–586 (2004).
7. C. Jing, Y. Fu, J. Huang, M. Zhang, Y. Yi, W. Gan, X. Xu, H. Shen, J. Lin, S. Zheng, J. Zhang, J. Zhou, J. Fan, Z. Ren, S. Qiu, and B. Zhang, "Prognostic nomogram based on histological characteristics of fibrotic tumor stroma in patients who underwent curative resection for intrahepatic cholangiocarcinoma," Oncologist **23**(12), 1482–1493 (2018).
8. M. W. Conklin and P. J. Keely, "Why the stroma matters in breast cancer: insights into breast cancer patient outcomes," Cell Adhes. Migr. **6**(3), 249–260 (2012).
9. E. M. De Kruijf, J. G. H. Van Nes, C. J. H. Van De Velde, H. Putter, V. T. H. B. M. Smit, G. J. Liefers, P. J. K. Kuppen, R. A. E. M. Tollenaar, and W. E. Mesker, "Tumor-stroma ratio in the primary tumor is a prognostic factor in early breast cancer patients, especially in triple-negative carcinoma patients," Breast Cancer Res. Treat. **125**(3), 687–696 (2011).
10. F. J. A. Gujam, J. Edwards, Z. M. A. Mohammed, J. J. Going, and D. C. McMillan, "The relationship between the tumour stroma percentage, clinicopathological characteristics and outcome in patients with operable ductal breast cancer," Br. J. Cancer **111**(1), 157–165 (2014).
11. C. L. Downey, S. A. Simpkins, J. White, D. L. Holliday, J. L. Jones, L. B. Jordan, J. Kulka, S. Pollock, S. S. Rajan, H. H. Thygesen, A. M. Hanby, and V. Speirs, "The prognostic significance of tumour-stroma ratio in oestrogen receptor-positive breast cancer," Br. J. Cancer **110**(7), 1744–1747 (2014).
12. C. L. Downey, H. H. Thygesen, N. Sharma, and A. M. Shaaban, "Prognostic significance of tumour stroma ratio in inflammatory breast cancer," SpringerPlus **4**(1), 68 (2015).
13. M. Van Bockstal, K. Lambein, A. Smeets, L. Slembrouck, P. Neven, I. Nevelsteen, C. Weltens, E. Van Limbergen, M. R. Christiaens, C. Van Ongeval, H. Wildiers, L. Libbrecht, and G. Floris, "Stromal characteristics are adequate prognosticators for recurrence risk in ductal carcinoma in situ of the breast," Eur. J. Surg. Oncol. **45**(4), 550–559 (2019).
14. C. J. H. Kramer, K. M. H. Vangangelt, G. W. van Pelt, T. J. A. Dekker, R. A. E. M. Tollenaar, and W. E. Mesker, "The prognostic value of tumour–stroma ratio in primary breast cancer with special attention to triple-negative tumours: a review," Breast Cancer Res. Treat. **173**(1), 55–64 (2019).
15. W. Jiang, J. Yan, M. Fu, W. Liu, G. Li, K. Li, X. Zheng, S. Zhuo, J. Lu, D. Chen, N. Zuo, S. Xu, J. Chen, W. Chen, D. Lin, J. Sui, Z. Liu, L. Chi, and G. Chen, "Association of the collagen signature in the tumor microenvironment with lymph node metastasis in early gastric cancer," JAMA Surg. **154**(3), e185249 (2019).
16. N. Ghosh and A. Vitkin, "Tissue polarimetry: concepts, challenges, applications, and outlook," J. Biomed. Opt. **16**(11), 110801 (2011).
17. V. V. Tuchin, "Polarized light interaction with tissues," J. Biomed. Opt. **21**(7), 071114 (2016).
18. M. Wolman, "Polarized light microscopy as a tool of of diagnostic pathology," J. Histochem. Cytochem. **23**(1), 21–50 (1975).
19. K. M. Woo, Y. Liu, A. Verma, K. W. Eliceiri, C. Drifka, A. Keikhosravi, and R. Oldenbourg, "Quantification of collagen organization in histopathology samples using liquid crystal based polarization microscopy," Biomed. Opt. Express **8**(9), 4243–4256 (2017).
20. N. M. Kalwani, C. A. Ong, A. C. Lysaght, S. J. Haward, G. H. McKinley, and K. M. Stankovic, "Quantitative polarized light microscopy of unstained mammalian cochlear sections," J. Biomed. Opt. **18**(2), 026021 (2013).
21. R. Oldenbourg, "Polarization microscopy with the LC-PolScope," in *Live Cell Imaging : A Laboratory Manual*, R. D. Goldman and D. L. Spector, eds. (Cold Spring Harbor Laboratory Press, 2005), pp. 205–237.
22. M. F. G. Wood, N. Vurgun, M. A. Wallenburg, and I. A. Vitkin, "Effects of formalin fixation on tissue optical polarization properties," Phys. Med. Biol. **56**(8), N115–N122 (2011).
23. Dennis H. Goldstein, *Polarized Light* (Marcel Dekker Inc, 2010).
24. S. A. Nelson, "Interference Phenomena, Compensation, and Optic Sign," *Tulane Univ. Mineral.*, 1–19 (2014).
25. U. Tatsuo, "Collagen fibers, reticular fibers and elastic fibers. A comprehensive understanding from a morphological viewpoint," Arch. Histol. Cytol. **65**(2), 109–126 (2002).
26. L. M. Wang, M. A. Silva, Z. D'Costa, R. Bockelmann, Z. Soonawalla, S. Liu, E. O'Neill, S. Mukherjee, W. G. McKenna, R. Muschel, and E. Fokas, "The prognostic role of desmoplastic stroma in pancreatic ductal adenocarcinoma," OncoTargets Ther. **7**(4), 4183–4194 (2016).
27. T. B. Halvorsen and E. Seimt, "Association between invasiveness, inflammatory reaction, desmoplasia and survival in colorectal cancer," J. Clin. Pathol. **42**(2), 162–166 (1989).
28. T. Morikawa, "Prognostic significance and molecular associations of tumor growth pattern in colorectal cancer," Ann Surg Oncol **19**(6), 1944–1953 (2012).
29. D. Layden, N. Ghosh, and A. Vitkin, "Quantitative polarimetry for tissue characterization and diagnosis," in *Advanced Biophotonics: Tissue Optical Sectioning* (CRC Press, 2013), pp. 459–494.
30. S. B. Mehta, "Polarized light imaging of birefringence and diattenuation at high resolution and high sensitivity," J. Opt. **15**(9), 094007 (2013).
31. W. E. Mesker, J. M. C. Junggeburt, K. Szuhai, P. de Heer, H. Morreau, H. J. Tanke, and R. A. E. M. Tollenaar, "The carcinoma-stromal ratio of colon carcinoma is an independent factor for survival compared to lymph node status and tumor stage," Cell. Oncol. **29**(5), 387–398 (2007).
32. X. C. Id, P. Simon, M. Jondet, and M. Vanhaeverbeek, "Quantification of stromal reaction in breast carcinoma and its correlation with tumor grade and free progression survival," PLoS One **14**(3), e0210263 (2019).